Large-scale computational design and simulation of viscoelastic metastructures for vibration attenuation

Robin Turlin [a,b], Thibaut Hirschler [a,b], Théo Calais [a,b], Hichem Seriket [a,b], Gaël Chevallier [c,d], Mahdi Bodaghi [e], Frédéric Demoly [a,b,f],*

[a] *Université Marie et Louis Pasteur, UTBM, CNRS, ICB UMR 6303, 90010 Belfort, France*
[b] *Université Bourgogne Europe, CNRS, ICB UMR 6303, 21000 Dijon, France*
[c] *Centre de recherche de l'École de l'air et de l'espace, École de l'air et de l'espace, 13660 Salon-de-Provence, France*
[d] *Université Marie et Louis Pasteur, CNRS, FEMTO-ST UMR 6174, 25000 Besançon, France*
[e] *Department of Engineering, School of Science and Technology, Nottingham Trent University, Nottingham, NG11 8NS, United Kingdom*
[f] *Institut universitaire de France (IUF), Paris, France*

ARTICLE INFO

ABSTRACT

Low-frequency vibration generated by rotating machinery in submarines pose a persistent challenge for acoustic stealth, as they are readily detected by passive sonar and are poorly mitigated by conventional passive or active control technologies under variable operating conditions. This paper introduces a scalable computational framework that couples shape-grammar-driven generative design with finite element simulations to systematically explore viscoelastic metastructures for vibration attenuation. The generative design method is defined by six dimension-independent geometric parameters, enabling automated synthesis of a broad and non-intuitive design space beyond traditional unit-cell parameterizations. Vibration transmissibility of each metastructure is quantified through numerical simulations, which are validated against experimental measurements on representative specimens. The results reveal viscoelastic metastructures exhibiting pronounced and tunable low-frequency attenuation bandwidths, therefore providing enhanced attenuation compared to conventional designs. The resulting dataset establishes a structured mapping between geometry and dynamic response, offering new insight into geometry-driven vibration mitigation mechanisms. Beyond forward analysis, the proposed framework provides a scalable foundation for data-driven and inverse design of metastructures targeting robust low-frequency vibration attenuation.

1. Introduction

Radiated noise poses a significant threat to submarine stealth as it can be captured by passive sonar, enabling tracking and identification. While substantial efforts have focused on mitigating external noise sources, such as propeller cavitation [1] and hull-fluid hydrodynamic interactions [2], at low operating speeds the radiated-noise signature is often dominated by structure-borne vibrations generated by onboard machinery [3]. Rotating machines are the primary sources of these vibrations, which produce broadband excitation under varying operating regimes. These vibrations propagate through air and solid paths, are transmitted via mounting systems, suspensions, and floating rafts, and ultimately radiate into the surrounding fluid through the hull [4–6].

Traditional vibration isolation relied on heavy mounting systems to ensure sufficient attenuation. However, weight reduction constraints have motivated the development of lightweight isolation concepts, including floating rafts inspired by lattice structures [7,8] and alternative

suspension technologies. Despite these advances, two major challenges remain relatively unresolved: achieving high attenuation levels (typically exceeding 20 dB) while effectively mitigating low-frequency vibrations without compromising static stiffness. Numerous vibration control strategies have been proposed to address these challenges [9], including distributed dynamic vibration absorbers (DVA) [10,11], locally resonant (LR) structures [12], particle dampers (PD) [13], quasi-zero-stiffness (QZS) systems [14], and active control approaches [15].

Several studies have shown that the trade-off between static stiffness and low-frequency attenuation can be partially controlled through thermal activation [16,17]. In addition, the resonance peak of the first mode can be mitigated using resonant metamaterials with a tailored distribution of internal resonance frequencies, without altering the static stiffness [18]. Bioinspired approaches have further expanded the design space. For example, Yan et al. [19] drew inspiration from insect leg to design a structure exhibiting modified QZS behavior, achieving

vibration isolation around 10 Hz. Similarly, Zhou et al. [20] investigated a limb-inspired QZS structure capable of attenuating vibrations at ultralow frequencies. Wu et al. [21], on the other hand, coupled electromagnetic active vibration control with QZS, drawing inspiration from a frog's morphology to enhance low-frequency attenuation. Despite this notable progress, most of these technologies tend to lose effectiveness under varying operating conditions, which leaves residual low-frequency radiation. Furthermore, although conventional mounts may provide attenuation at low frequencies, amplification often occurs at higher frequencies. Consequently, achieving reliable broadband vibration attenuation in variable environments remains a significant challenge [22].

Recent advances in additive manufacturing have enabled the fabrication of complex geometries, renewing interest in mechanical metamaterials and metastructures that combine lightweight design and tailored mechanical responses. Metamaterials derive unusual properties from their microstructure, whereas metastructures achieve functional performance primarily through architectural design. These concepts have been successfully applied to acoustic insulation [23,24], cloaking, energy absorption, and vibration attenuation [25,26]. In the context of vibration isolation, lattice structures – including auxetic [27, 28], chiral [29–31], origami-inspired [32], bio-inspired [33–35], and sandwich-type designs [36–39] – have demonstrated promising attenuation capabilities across low- and mid-frequency ranges [40].

Among these approaches, many metamaterials and metastructures have been developed using the two most widely adopted concepts: QZS and LR. A classical QZS metastructure was introduced by Fan et al. [41], who designed a 2D structure composed of sinusoidal beams to achieve QZS behavior and low-frequency vibration attenuation. Building on this concept, Zhao [42] developed 1D QZS structure using curved beams, then applied mirror operations to obtain a 2D configuration, and finally translated the geometry in space to generate a 3D QZS metastructure. Zhou et al. [43] and He et al. [44] explored QZS metastructures inspired by origami principles, therefore achieving low-frequency vibration attenuation. Later, Liu et al. [45] and Li et al. [46] proposed novel 3D QZS metastructures composed of curved beams. In particular, Li et al. [46] introduced an arched beam connected to the base of the unit cell to achieve unidirectional behavior by rotating the unit cell by 90°, resulting in vibration isolation from 20 Hz up to 6 kHz. Using curved beams as well, Liu et al. [47] proposed a cylindrical QZS metastructure in which each level consisted of four pairs of curved beams, an they investigated how added mass influenced transmissibility performance. Bioinspired approaches have also been explored. Ravanbod et al. [48] proposed a 3D QZS metastructure inspired by the tongue of woodpecker, which achieved effective vibration attenuation. Furthermore, Lin et al. [49] and Cai et al. [50] introduced metamaterials coupling QZS and LR principles, where the curved beams acted as springs and internal structures served as local masses, thereby enabling vibration attenuation below 500 Hz.

LR metamaterials and metastructures have likewise been extensively studied for vibration mitigation. For instance, Jiang et al. [51] and d. Li et al. [52] designed cubic unit cells connected by struts, leading respectively to vibration attenuation between 400 Hz and 1.5 kHz and multiple attenuation bands in the kilohertz range, respectively. Using LR principles, Li and Yan [53] proposed a chiral auxetic structure incorporating local resonators to obtain multiple attenuation regions between 0 and 5 kHz. Jiang et al. [54] embedded spherical masses within the cellular unit cells to induce vibration mitigation around 2 kHz. Following a similar strategy, Abubakar et al. [55] designed a 3D cubic re-entrant metamaterial with embedded masses and studied their influence on vibration mitigation performance. Wu et al. [56] subsequently resized a 3D re-entrant unit cell to function as a local resonator and investigated the influence of material properties on vibration isolation. Beyond cellular structures, tires have also shown potential for attenuation [57,58]. Wang et al. [59] further proposed a locally resonant metastructure inspired by a spider, combining an origami-based main body with a central mass. Numerous other LR designs have been proposed, including beam lattices, syndiotactic chiral structures, and unit cells containing embedded masses [60–64].

Lightweight solutions such as sandwich structures [65] and periodic lattice exhibiting LR effects [66] have also been proposed as alternatives to traditional mounting systems and floating rafts. Similarly, Yang et al. [67] introduced a particle damper composed of a lattice filled with granular material to enhance vibration mitigation. Gao et al. [68] proposed a re-entrant lattice with particles placed at the vertices to enable low-frequency vibration mitigation. By coupling multiple dissipation mechanisms, Tomita et al. [69] developed a plate-based metamaterial combining local resonators with embedded particles, therefore achieving significant mitigation around 200 Hz.

While these designs may exhibit strong performance individually or when integrated with conventional mounting technologies, exhaustively exploring the full design space via physical prototyping and experimental testing remains challenging. Therefore, there is a need for efficient strategies to investigate structural configurations exhibiting diverse dynamic behaviors across the frequency range of interest. One promising approach is the creation of a systematic dataset in which each geometry is paired with its corresponding performance metrics. Such a dataset is fundamental for inverse design, which aims to navigate large design spaces to identify optimal solutions. In the physical sciences, datasets have been successfully employed to model properties such as energy absorption [70] and acoustic attenuation [71].

Various design strategies have been proposed in this context. Some rely on control points to define geometries, as in QZS isolators [72] or unit-cell vertex parameterizations [73]. Others adjusted chiral-cell dimensions [74,75], or applied binary material distributions at the unit-cell scale [76–78]. Generative design offers an alternative framework [79], encompassing topology optimization [80,81], machine-learning-based generation [82], and grammar-based methods such as L-systems [83,84], graph grammars [85], and shape grammars. However, topology optimization typically targets a single optimal solution for a predefined objective, making it unsuitable for generating large populations of distinct lattice designs. Machine-learning-based generation holds great promise but is strongly dependent on the quality and printability of the initial dataset, which can limit its applicability in inverse design problems. Grammar-based methods provide a compelling alternative: L-systems are generally restricted to fractal lattices, while graph grammars focus primarily on strut-based lattices. Shape grammars, in contrast, enable rule-based geometric transformations of predefined objects and have demonstrated versatility across architecture [86], product design [87], and engineering [88,89].

In this work, we propose a large-scale computational framework integrating shape-grammar-driven generative design with finite element (FE) analysis to systematically explore viscoelastic metastructures for vibration attenuation. Unit-cell geometries are parameterized using up to six dimension-independant geometric variables and assembled into metastructures through a set of grammar rules. This enables the automated generation of thousands of distinct structural designs through a design generator implemented in Rhinoceros 3D/Grasshopper® environment. Vibration transmissibility is evaluated using FE simulations implemented in the open-source FEniCSx platform, and selected configurations are validated experimentally. The resulting dataset establishes a structured relationship between geometry and dynamic response, which provides new insights into geometry-driven vibration attenuation and laying out the foundation for future data-driven and inverse design strategies.

The remainder of the paper is organized as follows. Section 2 details the generative design method. Section 3 presents the modeling approach, numerical implementation, and experimental validation. Section 4 introduces the digital pipeline used to build the large-scale metastructure dataset for vibration attenuation.
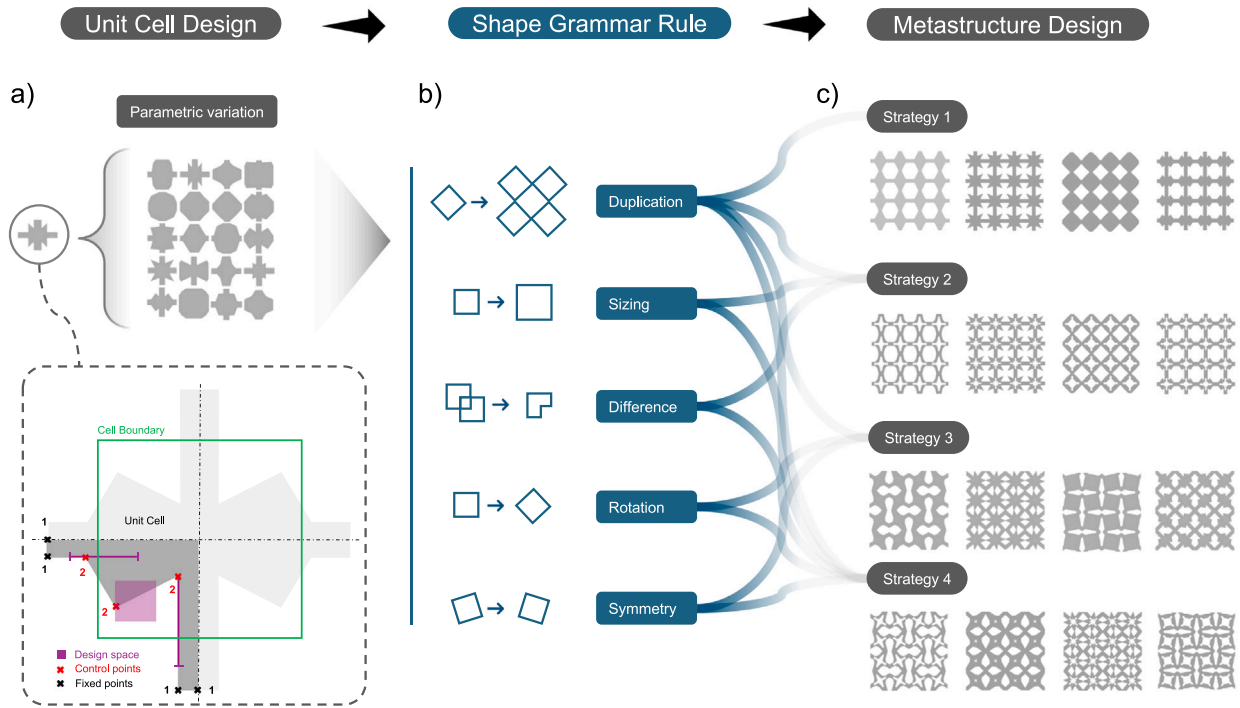
Fig. 1. Generative design workflow of metastructures using shape grammar rules: (a) unit cell design space and example of variants; (b) shape grammar rules definition; (c) design strategies leading to different metastructure configurations.

2. Generative design methodology

The systematic exploration of metastructures and their vibration attenuation performance requires an appropriate generative design approach. In this work, we propose a bottom-up strategy that begins with the parameterization of a unit cell and progressively extends to more complex structures through the successive application of shape grammar rules. This approach is similar to layered shape grammar [90], where each additional rule incrementally increases geometric complexity. Fig. 1 gives an overview of the proposed generative design methodology to build a large collection of metastructures suitable for vibration attenuation. Each step of the approach is described in the following subsections. Further technical details are left to Appendix B.

2.1. Unit cell design

The systemic design of metastructures follows a structured workflow beginning at the unit cell level. As illustrated in Fig. 1a, the design space is first defined by a bounded square domain, representing the elementary unit of repetition. To ensure scalability and reduce design complexity, symmetric constraints are introduced, which limit the number of independent control parameters while ensuring seamless interfaces between adjacent cells. Within the constrained domain, two categories of control points are defined: fixed points, placed outside the unit cell boundaries to ensure structural continuity across adjacent cells, even under rotation, and variable points, which parameterize the unit cell geometry. The variable points span bounded ranges, enabling controlled variation while preventing degenerate or unstable configurations. Two of these can move both inside and outside the unit cell, resulting in geometries with variable stiffness and interface lengths. An additional control point is positioned within a smaller square domain centered in the unit cell. When its two endpoints define a diagonal that serves as a symmetry axis, reflecting a point located in the upper half of the domain produces a rotated version of the original unit cell. If the

variables of the two peripheral control points are equal, this operation yields the same geometry rotated by 90°, thereby eliminating the need to explicitly perform rotational transformations to explore such configurations within the design space. Moreover, when the central control point lies directly on the diagonal and the other variables remain equal, the unit cell exhibits four symmetrical planes. This parameterization created a vast but finite design space, thus enabling both systematic exploration and data-driven approaches like machine learning. Once the control points are specified, a sequence of shape grammar rules is applied to generate candidate geometries. These rules include (i) connection rules linking the control points, (ii) symmetry rules replicating and reflecting the geometry according to the imposed symmetry planes, and (iii) intersection rules trimming the resulting shape to the predefined design domain. The systemic application of these rules transforms abstract parameters into concrete unit cell geometries. The use of straight lines to connect control points, rather than splines, was motivated by practical considerations. In preliminary tests, splines interpolation tended to oversmooth the geometry, thus reducing geometric diversity for a given control-point configuration. Moreover, when scaled down, curved contours frequently intersected with the original shape, compromising geometric validity of the dataset. The adopted parameterization and associated rule set therefore represent a trade-off between geometric richness and dataset stability. Examples of the resulting cells, including special symmetric cases, are shown in Fig. 1c.

2.2. Shape grammar rules

Within the design framework, shape grammar rules constitute the core mechanism that governs the generation and transformation of unit cell geometries. Rather than being viewed as isolated geometric operations, these rules act as formalized procedures that enabled the controlled evolution of an initial unit cell into increasingly complex configurations. They ensure that design variation is not arbitrary but

instead follows a consistent and reproducible logic, therefore making them essential for generative and systematic design approaches. Here, the design workflow is structured around a set of fundamental shape grammar rules, such as illustrated in Fig. 1b and described hereafter:

- *Rotation* — reorients a geometry within its domain without altering its structural identity, preserving systematic coherence across the design space. This operation is characterized by a specified axis within a defined plane, and a given angle.
- *Sizing* — scales a geometry while maintaining proportional integrity, enabling systematic exploration of structural hierarchies.
- *Difference* — removes overlapping regions between shapes, creating voids or substructures that enrich diversity.
- *Symmetry* — generates mirrored counterparts across reference planes, ensuring continuity.
- *Duplication* — replicates shapes along spatial axes according to controlled parameters, enabling repetition and modularity in metastructures.

2.3. Design of 2D metastructures

Through this generative design framework, and considering the designed unit cell, four distinct strategies are introduced to generate periodic 2D metastructures. Each strategy, illustrated in Fig. 1c, represents a different pathway through the shape grammar rules workflow, ranging from the most elementary to the most complex configuration, as follows:

- *Strategy 1 — Direct Duplication.* The simplest pathway applies the duplication rule immediately after the design of the unit cell. This generates periodic repetitions across the design domain, producing the first class of metastructures. Here, the geometry is entirely determined by the positions of the variable control points, requiring only four design parameters.
- *Strategy 2 — Cavity formation by sizing and difference.* Complexity is increased by introducing a sizing rule followed by a difference operation, which reduces the initial unit cell and subtracts it from its original geometry, creating cavities. Applying duplication afterward produces lightweight lattices with tunable porosity. An additional sizing parameter extends the design space to five dimensions, with cavity size directly influencing structural weight.
- *Strategy 3 — Rotation with symmetry correction.* Another pathway integrates rotation into the workflow. Since rotation alone disrupts continuity between neighboring cells, the geometry is subsequently restored through symmetry operations. The imposed symmetry planes ensure structural compatibility while constraining the rotation angle between 0° and 90°. This introduces the rotation angle as a fifth parameter, yielding metastructures with directional anisotropy and controlled variation.
- *Strategy 4 — Combined sizing, difference, symmetry, and rotation.* The most complex pathway merges the cavity-forming and rotation strategies. Here, the design process is governed by six independent parameters, generating a large set of configurations. This hybrid approach illustrates the full integrity of the design workflow, combining lightweighting and directional tailoring.

Taken together, these strategies demonstrate how the systematic application of shapes grammar rules – i.e., duplication, sizing, difference, rotation, and symmetry – enables scalable exploration of the design space. The method balances simplicity and complexity, therefore providing a structured way to navigate from four-parameter unit cells to highly configurable metastructures. Let us finally refer to Appendix B where some of the technical aspects of the generative design methodology are further detailed, and some extensions to 3D metastructures are discussed.

3. Transmissibility computation

This section presents the numerical framework developed to compute the transmissibility of each designed metastructure, each enabling systematic quantification of vibration attenuation efficiency across the generated geometries. The methodology integrates high-fidelity FE analysis with a compact design-to-simulation workflow and is validated against experimental data.

3.1. Definition

Here, the transmissibility $T : \mathbb{R}_+ \to \mathbb{R}$ of the metastructures is assessed using a simple mounting system [91], quantifying the ratio between the output U_{out} and input U_{in} displacement magnitudes under harmonic excitation:

$$T(\omega) = \frac{U_{\text{out}}(\omega)}{U_{\text{in}}}, \tag{1}$$

where ω is the excitation angular frequency. It serves as a measure of the structure's ability to isolate or amplify vibrations across frequency ranges, as illustrated in Fig. 2.

For a simple mounting system, the frequency response of the system can be divided into three regimes (see again the example depicted in Fig. 2). At low frequencies, the transmissibility $T(\omega)$ is approximately equal to one, indicating that the supported mass follows the imposed motion without significant amplification or attenuation. This behavior is typically referred to as rigid-body motion. As the frequency increases, the system may enter a resonance regime characterized by $T(\omega) > 1$ (or even $T(\omega) \gg 1$), where the output amplitude exceeds the input and a resonance peak appears before the response begins to decrease. Beyond this point, the transmissibility drops below one, marking the beginning of the attenuation regime. In this final regime, the metastructure effectively filters out vibrations. In what follows, we consider that when the metastructure has interesting vibration absorption properties $T(\omega) < 10^{-2}$.

3.2. Numerical modeling of the mounting system

The evaluation of the transmissibility of a metastructure is done numerically, based on the model illustrated in Fig. 2a. It involves a FE model of the metastructure (i.e., the antivibration mount) coupled to a rigid body model of the mounting mass.

Formulation. More specifically, the metastructure is modeled as a viscoelastic continuum with material parameters: storage modulus E, Poisson's ratio ν, loss factor η, and density ρ. We assume small displacements and denote by $\boldsymbol{u}_1 : (\Omega_1, \mathbb{R}_+) \to \mathbb{C}^d$ the displacement field within the metastructure domain $\Omega^1 \subset \mathbb{R}^d$. We also assume plane strains for 2D configurations (i.e., when the spatial dimension $d = 2$). The bottom side (or the input side) of the metastructure, defined by Γ_b (see also Fig. 2(a)), is subjected to a harmonic displacement in the y-direction. In addition, the metastructure supports an item of mass. This mounted item is assumed to be a rigid body of mass m_2 and inertia tensor $\mathbf{I}_2$ measured relative to its center of mass. We denote by $\boldsymbol{u}_2 : \mathbb{R}_+ \to \mathbb{C}^d$ and $\boldsymbol{\theta}_2 : \mathbb{R}_+ \to \mathbb{C}^d$ the displacements and rotations of the mounting item, expressed at the center of mass as well. We assume a perfect coupling between the metastructure and the item of mass at their interface Γ_t (Fig. 2). The overall vibration problem to be solved reads as follows. We are looking for $\boldsymbol{u}_1$, $\boldsymbol{u}_2$ and $\boldsymbol{\theta}_2$ solutions of:

[Balance] $\qquad \rho_1 \ddot{\boldsymbol{u}}_1(\text{x},t) = \text{div}(\boldsymbol{\sigma}_1(\text{x},t)), \qquad$ in $\Omega_1,$ (2a)

[Constitutive law] $\qquad \boldsymbol{\sigma}_1(\text{x},t) = (1+i\eta)\mathbf{C} : \boldsymbol{\varepsilon}(\boldsymbol{u}_1(\text{x},t)), \quad$ in $\Omega_1,$ (2b)

[Euler's first law] $\qquad m_2 \ddot{\boldsymbol{u}}_2(t) = -\int_{\Gamma_t} \boldsymbol{\sigma}_1 \cdot \boldsymbol{n} \, dl,$ (2c)

[Euler's second law] $\qquad \mathbf{I}_2 \ddot{\boldsymbol{\theta}}_2(t) = -\int_{\Gamma_t} (\boldsymbol{\sigma}_1 \cdot \boldsymbol{n}) \times \boldsymbol{r} \, dl,$ (2d)
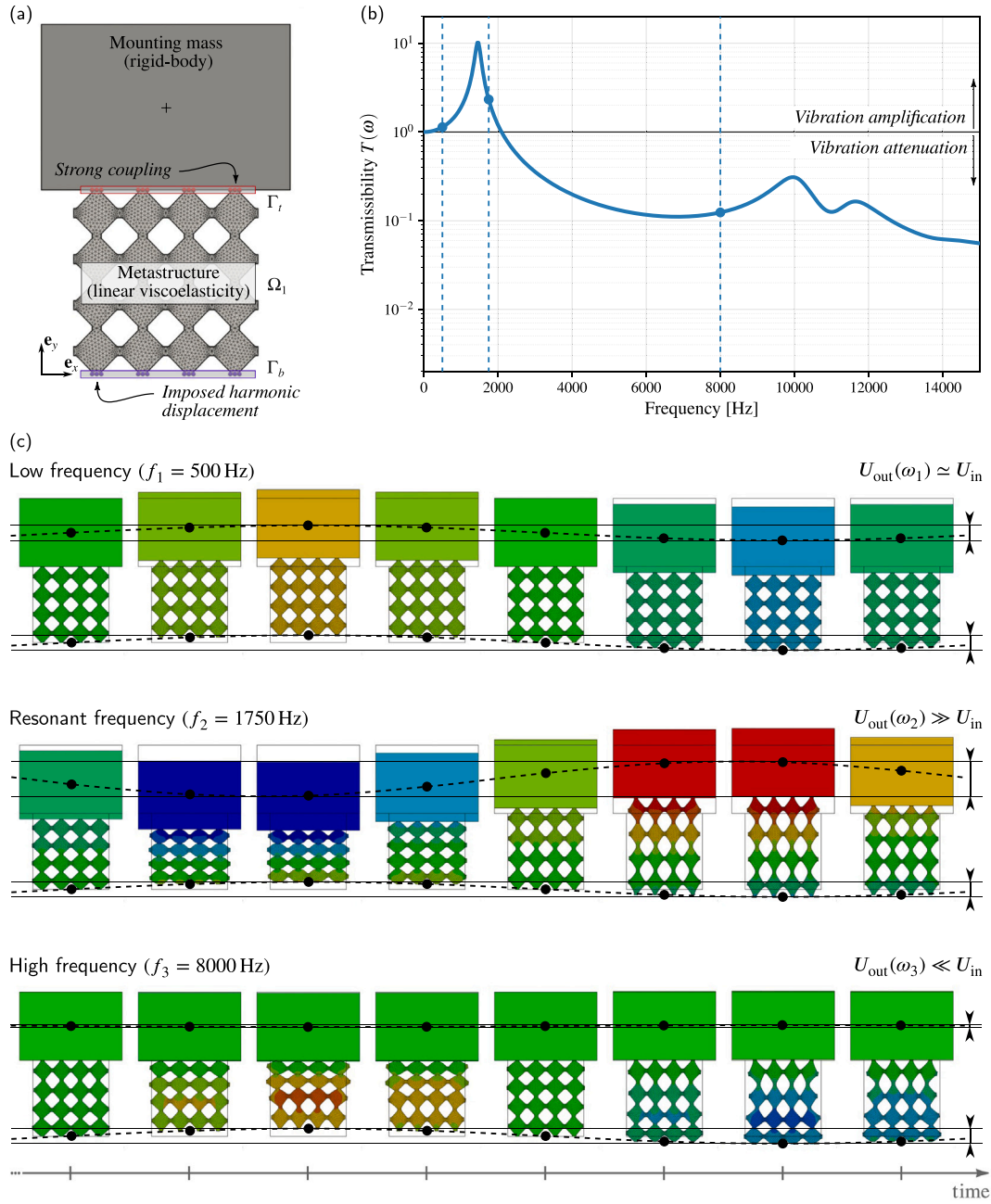
Fig. 2. Modeling and transmissibility analysis of a simple mounting system. (a) FE model of the considered problem, (b) Plot of the transmissibility w.r.t. the excitation frequency associated to the metastructure on the left, and (c) FE results showing the time-dependent deformed configuration for different frequencies (note: the colormap is associated to the vertical displacement).

[Continuity of the disp.] $\quad \boldsymbol{u}_1(\mathrm{x},\mathrm{t}) = \boldsymbol{u}_2(\mathrm{t}) + \boldsymbol{\theta}_2(\mathrm{t}) \times \boldsymbol{r}(\mathrm{x}),\quad$ over $\Gamma_t,\quad$ (2e)

[Imposed harmonic disp.] $\quad \boldsymbol{u}_1(\mathrm{x},\mathrm{t}) = U_{\mathrm{in}}\exp(\mathrm{i}\omega\mathrm{t})\mathbf{e}_y,\quad$ over $\Gamma_b,\quad$ (2f)

where σ, ε are respectively the linearized Cauchy stress and Green–Lagrange strain tensors, $\mathbf{C}$ is the Hooke material tensor, $\boldsymbol{n}$ is the outward unit normal to Ω_1, and $\boldsymbol{r}$ the distance vector from points on Γ_t to the center of mass G of the mounting item. The output vibration magnitude is measured from the vertical displacement of this item of mass, i.e., $U_{\mathrm{out}}(\omega) = |\mathbf{u}_2(\omega) \cdot \mathbf{e}_y|$.

Numerical solution. Problem (2) is solved classically by using the FE method (first-order Lagrange triangular elements) together with modal superposition. In practice, it leads to complex-valued linear systems of equations of the following form:

$$\bar{\mathbf{D}}(\omega)\,\mathbf{d}^{\mathrm{rel}} = \omega^2 \bar{\mathbf{M}}\,\mathbf{d}^0, \tag{3}$$

where $\bar{\mathbf{D}}(\omega)$ and $\bar{\mathbf{M}}$ denote the dynamic stiffness and mass matrices, respectively. The displacement and rotation unknowns contained in vector $\mathbf{d}^{\mathrm{rel}}$ are obtained by solving (3) approximately based on a set of eigenmodes $(\omega_k, \mathbf{v}_k)$, as follows:

$$\mathbf{d}^{\mathrm{rel}}(\omega) \approx \sum_{k=1}^{n_M} \mathbf{v}_k\,\alpha_k(\omega),\quad \text{with}\quad \alpha_k(\omega) = \mathbf{v}_k^\mathsf{T}\bar{\mathbf{M}}\,\mathbf{d}^0\,\frac{\omega^2}{(1+\mathrm{i}\eta)\omega_k^2 - \omega^2}.$$

For more details on the different operators and quantities involved in this numerical model, see Appendix A.
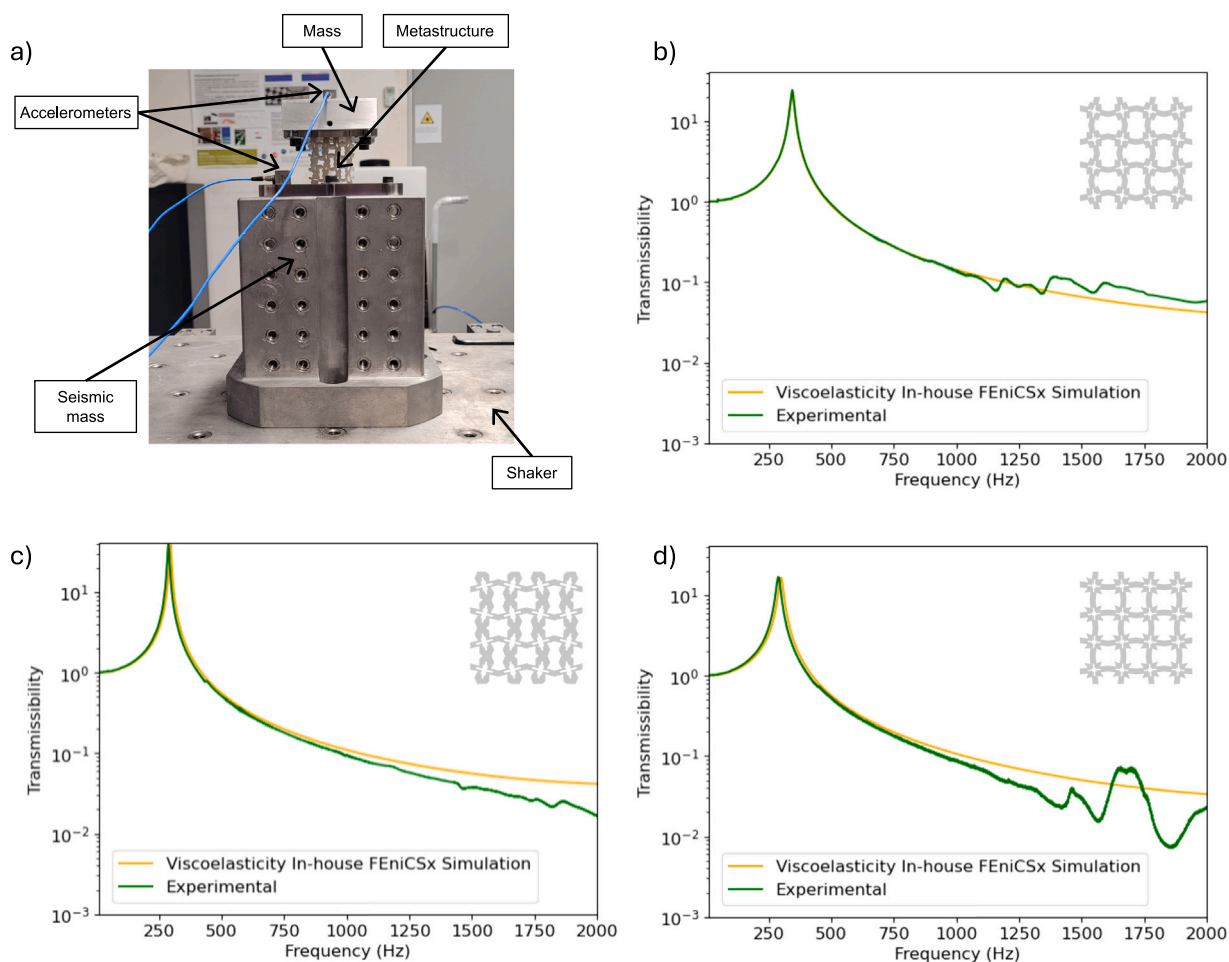
Fig. 3. Experimental framework for transmissibility analysis. (a) Experimental setup employed to measure vibration transmissibility and validate the numerical model with the geometric model of the metastructure used for simulations and experimentation; (b) to (d) Comparisons of simulated and measured transmissibility curves for three distinct metastructures, demonstrating the model's predictive accuracy.

Implementation details. The full computational workflow is automated as follows. First, the geometry generation of metastructures is implemented within the Rhinoceros 3D (Version 7)/Grasshopper® environment using the shape grammar rules described in Section 2.2. Generated geometries are then exported in STEP files and meshed using GMSH [92]. The steady-state dynamic analysis is implemented using the open-source FE platform FEniCSx [93], where harmonic excitation is applied and the transmissibility is evaluated. This systematic simulation pipeline enables high-throughput computation of vibration transmissibility, forming the foundation of the large dataset used for subsequent data-driven and inverse design studies.

3.3. Experimental validation

The final stage of the computational design methodology involves validating the numerical model through direct comparison with experimental measurements. This crucial step ensures that the simulation framework used to compute the transmissibility accurately captures the physical behavior of the metastructures designed in the previous stages.

The experimental setup is presented in Fig. 3a. The metastructure is fixed to the mounting mass and to the seismic mass through two intermediate regions, added at the top and bottom parts of the metastructure. This enables to screw and align the metastructure to the mounting mass (top interface) and to the shaker (or the seismic mass, bottom interface). The metastructure and the intermediate regions are manufactured as a single part using 3D printing with PolyJet™

technology, based on the commercial VeroClear™ material. For this experimental validation, we printed three metastructures generated using Strategy 4 (see Section 2.3). The mounting mass consists in a 80 mm × 80 mm × 25 mm aluminum block. The input acceleration was recorded using an accelerometer attached to the shaker, whereas the output response was measured with another accelerometer placed on the upper surface of the mass, see again Fig. 3(a). Based on the measurements, the transmissibility is evaluated as the ratio of the output-to-input acceleration amplitudes over the frequency range. The transmissibility of the three tested metastructures are depicted on Figs. 3 b, c, and d.

Along with these experimental results, Fig. 3 also presents the numerical results for the three designs. The material parameters used for the simulation are a Young's modulus $E = 1.2\,\text{GPa}$, Poisson's ratio $\nu = 0.312$, and density $\rho = 1.18\,\text{g mm}^{-3}$, identified through additional in-house mechanical tests. A good agreement between the experimental and numerical results is observed. Especially, the relative error in terms of resonant frequencies are 0.32 %, 3.1 % and 4.1 % for the three studied designs, respectively. It remains the question of the loss factor. Indeed, one can notice that the maximal resonance peaks are slightly different for each structure. Thus, one would require different values of loss factors to capture these maximal transmissibilities accurately. This has been done in the results presented in Fig. 3 where the loss factor is set as $\eta = 0.045$, 0.025 and 0.06, respectively. Additionally, let us note that the current experimental setup does not allow us to measure the transmissibility above 2 kHz. Therefore, we choose to identify a
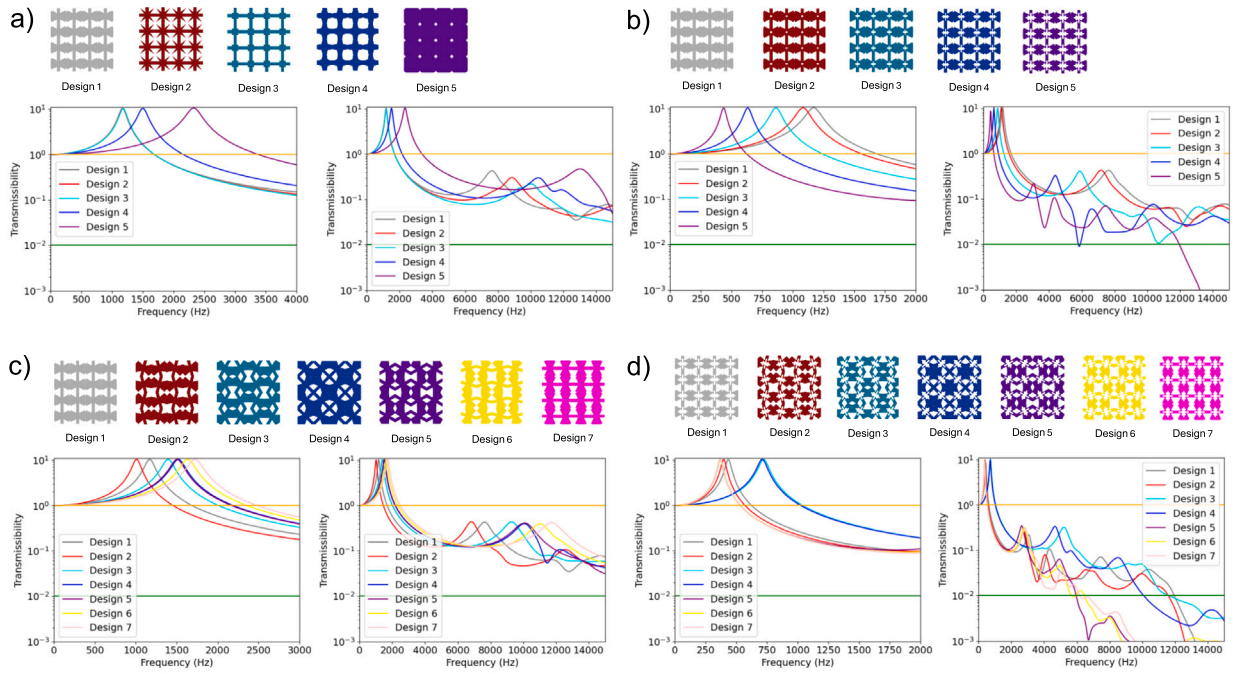
Fig. 4. Influence of shape grammar rules influence on the transmissibility of metastructures for different construction strategies: (a) Strategy 1, (b) Strategy 2, (c) Strategy 3, and (d) Strategy 4. Each strategy is evaluated over two frequency ranges to highlight low- and high-frequency behavior.

constant loss factor based on these experimental results and not to introduce a frequency-dependent loss factor in our numerical model. Furthermore, we select a single value $\eta = 0.1$ during the dataset construction (see Section 4.2), mainly for the sake of simplicity. The value of the loss factor principally influences the maximal peaks, but less the general shape of the transmissibility curve and the values of resonant frequencies. Therefore, we believe that such a constant loss factor is valid in our context of design-related investigations.

4. Results and discussion

This section explores how the previously generated metastructures influence the corresponding mechanical and dynamic behaviors. The first part examines the influence of successively applied shape grammar rules, demonstrating that each additional rule not only modifies the dynamic response but also promotes the emergence of low transmissibility while enriching the diversity of mechanical performance. The second part focuses on constructing the complete dataset and analyzing the transmissibility characteristics of the resulting lattice configurations.

4.1. Influence of layered shape grammar rules on transmissibility performance

Increasing the number of applied shape grammar rules systematically enhances the geometric and mechanical complexity of the metastructures. To quantify this effect, transmissibility analyses were performed on 2D metastructures corresponding to different design layers. To illustrate the variability introduced by the simplest configuration, five metastructures were examined using only the duplication rule. The first design corresponds to the reference unit cell introduced in the design methodology, while the remaining four represent geometric extrema within the design space.

Fig. 4a presents their transmissibility responses over two frequency ranges. The first plot divided into two graphs covering different frequency ranges. The first plot (0–4 kHz) highlights the resonance behavior. The stiffest design (Design 5) exhibits the highest resonance frequency, reaching approximately 2.4 kHz, whereas the lighter, more compliant designs resonate near 1.2 kHz. This confirms the expected

relationship between stiffness and resonance frequency (remember that for an one DOF spring-mass system (k, m), the natural frequency is given by $\omega_0 = \sqrt{k/m}$). Beyond 3 kHz, significant divergence appears between designs, as shown in the second plot. While all designed metastructures exhibit attenuation behavior at higher frequencies — initiating around 1.7 kHz for the first three designs, 2.25 kHz for the fourth, and 3.3 kHz for the fifth. The orange line in the figure indicates the attenuation threshold $(T = 1)$, while the green line marks the objective $(T < 0.01)$. As observed, none of the designs crosses this threshold up to 15 kHz, confirming that the duplication rule alone cannot achieve the attenuation targeted in the frequency range studied.

The rotation angle represents a key parameter that governs both the geometry and the mechanical anisotropy of the metastructure. Fig. 4(b) shows the transmissibility for metastructures rotated by 0°, 15°, 30°, 45°, 60°, 75°, and 90°. The first and last designs exhibit markedly distinct transmissibility curves, highlighting the anisotropic nature of the metastructure. In contrast, unit cells with four planes of symmetry would yield identical responses for rotations of 0° and 90°. Rotation modifies the material distribution and, consequently, the effective stiffness of the metastructure. In this case, increasing the rotation angle results in stiffer structures. The fourth and fifth designs, which differ geometrically, resonate both near 1.5 kHz but exhibit distinct high-frequency behaviors. Although none of the rotated designs achieve the targeted vibration attenuation within the studied frequency range, the variation in transmissibility confirms that rotation effectively tunes stiffness and material distribution, serving as a valuable means of adjusting dynamic behavior without altering the underlying geometry or topology of the unit cell.

The influence of the sizing rule on transmissibility is illustrated in Fig. 4c. The first design corresponds to the baseline metastructure, while the others incorporate sizing parameters of 0.1, 0.2, 0.3, and 0.4, where 0.1 and 0.4 represent the lower and upper bounds of the parameter range. As the sizing parameter increases, the metastructure becomes more compliant, leading to sharper and more pronounced resonance peaks. Moreover, the resonance frequency shifts toward lower values: the unsized metastructure resonates around 1.2 kHz, while the most compliant design (sizing = 0.4) resonates near 400 Hz. The smallest sizing value produces a response nearly identical to the
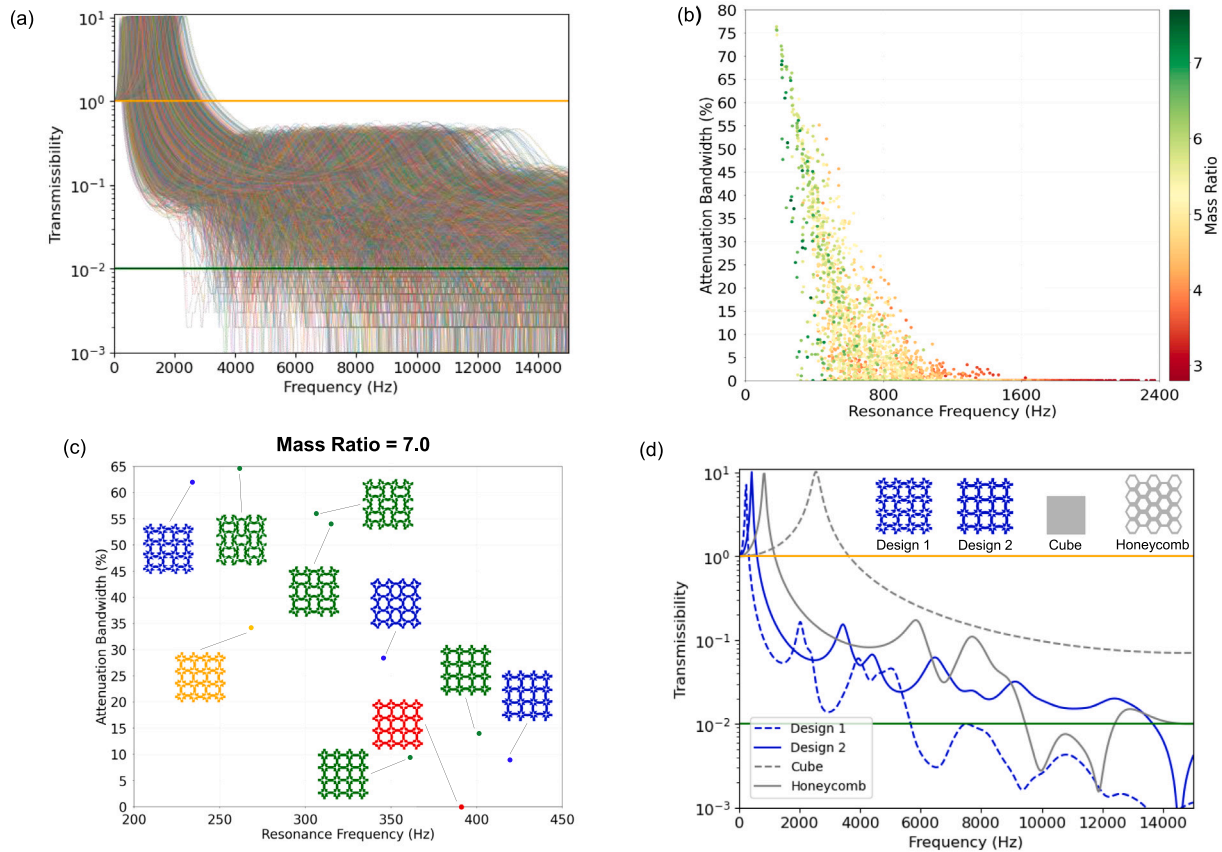
Fig. 5. Dataset performance overview. (a) Transmissibility curves for the complete set of simulated metastructures, illustrating the diversity of dynamic responses across the dataset. (b) 2D design space representing the relationships between the attenuation bandwidth, resonance frequency, with each metastructure colored by its corresponding mass ratio feature, highlighting the distribution of generated designs. (c) 2D projection of the design space for a fixed mass ratio of 7.0, showing representative metastructures color-coded by the number of absorption bandwidth (red: none, blue: one, green: two, orange: three). (d) Comparison of the transmissibility curves for the best- and worst- performing designs within the subset of metastructures having a mass ratio of 7.0 with traditional designs, demonstrating the strong influence of resonance frequency and total bandwidth on vibration attenuation performance.

baseline design, as expected from their similar geometries. In the high-frequency domain, transmissibility curves exhibit comparable trends; however, metastructures with higher sizing parameters display more efficient filtering behavior. A narrow absorption bandwidth appears around 4 kHz for a sizing of 0.3, while a wider one (~3 kHz) emerges above 12 kHz for the 0.4 configuration. These results suggest that larger sizing parameters promote both the formation and widening of absorption bandwidth while lowering resonance frequencies, therefore demonstrating the critical role of sizing in tailoring metastructure dynamics.

After independently analyzing the effects of the sizing and rotation shape grammar rules, the final strategy assesses their coupled influence on transmissibility performance (Fig. 4d). In this strategy (i.e., Strategy 4), the sizing parameter is set to its maximum value, while the rotation angle varies according to the same increments used in the previous analysis. In the low-frequency domain, two designs exhibit resonance peaks near 700 Hz, whereas the other strategies reach resonance between 300 and 400 Hz. More importantly, all designs resulting from the construction Strategy 4 display at least one wide absorption bandwidth. The first design shows a absorption bandwidth initiating at 12 kHz, while the second and third present similar attenuation starting near 11.8 kHz. The Design 4 reaches this regime around 10 kHz. The last three designs (i.e., Design 5, Design 6, and Design 7) are particularly notable, with absorption bandwidth emerging as low as 6 kHz. These results demonstrate that increasing the complexity of the metastructure through the successive application of shape grammar rules enriches the diversity of transmissibility profiles and enhances overall dynamic

performance. Owing to its superior attenuation performance, this final strategy has been selected as the reference architecture for constructing the large-scale dataset.

4.2. Dataset construction

The first step in constructing the large-scale dataset consisted of generating the full set of geometries serving as its foundation. This was achieved using a Python script developed within the Rhinoceros 7/Grasshopper® environment. Each generated metastructure was exported as a STEP file, while the associated design parameters – including the four geometric coordinates, the sizing parameter, and the rotation angle – were recorded in a CSV file sharing the same identifier as the corresponding geometry. All geometries were subsequently processed though an in-house numerical simulation workflow. While geometry generation required only about one second for two designs, each simulation took approximately ten seconds per metastructure. This step yielded not only the transmissibility curve but also key dynamic metrics, including the resonance frequency, the number of absorption bandwidth, and the attenuation band — defined as the cumulative number of frequency where the transmissibility remains below 0.01. Additionally, the mass ratio, defined as the ratio between the masses of the mounting item and the metastructure, was also computed.

A total of 5000 metastructures were generated and simulated (see **Movie S1**). Fig. 5a shows all resulting transmissibility curves, where numerous configurations already exhibit clear absorption bandwidth. Among the 5000 tested structures, 1665 presented at least one absorption bandwidth: 1221 had a single absorption bandwidth, 367 exhibited

two, 67 show three, and 10 revealed four distinct absorption bandwidths. However, the presence of multiple absorption bandwidths does not necessarily ensure efficient vibration attenuation of the mounted component. To better visualize the overall performance landscape, a two-dimensional design space independent of the number of absorption bandwidths was constructed and shown in Fig. 5b. The *x*- and *y*-axes correspond to the resonance frequency and total bandwidth, while the color of each point represents the metastructure's mass ratio. Within this dataset, resonance frequencies ranged from 179 Hz to 2370.8 Hz, attenuation range varied from 0 % (for configurations with no bandwidth) to up to 76.67 %, and the mass ratio spanned from 2.8 to 7.7. The resulting design space included structures exhibiting no absorption bandwidth, which are readily identified by their attenuation range equal to 0 %. To explore the design space, a visualization tool called Meta Explorer was developed, and its functionality is detailed in **Supplementary Materials** (see also **Movie S1**). This tool allows direct identification of the geometry associated with different physical parameters. Most generated metastructures clustered in the region characterized by small attenuation bandwidth, high resonance frequencies, and low mass ratios, corresponding to high-stiffness geometries with dense material distributions. Conversely, fewer metastructures exhibited the desirable combination of low resonance frequency, high attenuation range percentage, and high mass ratio, which are typically associated with more compliant and efficiently attenuating designs. As highlighted by Snowdon [91], a structure exhibiting a favorable transmissibility curve does not necessarily perform effectively in vibration isolation if it lacks a sufficiently high mass ratio. In the generated dataset, all geometries with a mass ratio equal or superior to 6 possess low resonance frequency and many of them also have great attenuation bandwidth with some superior to 60 %, making them great candidates compare to those with a mass ratio inferior to 6. Consequently, even if the structure has a lower mass ratio compare to best-performing structure with a mass ratio of 7.7, they can be considered as potential candidates. However, structures with a mass ratio inferior to 5 tends to have a high resonance frequency and an attenuation bandwith inferior to 30 %. Therefore, metastructures with low mass ratios were excluded from further analyses, focusing instead on those exhibiting high ratios.

Among the top-performing designs, one metastructure achieved the maximum mass ratio of 7.7. Several other metastructures displayed comparable performance, with three metastructures reaching a ratio of 7.5 and ten achieved 7.0. Fig. 5c illustrates the metastructures whose geometries were identified almost instantly using Meta Explorer within a 2D projection of the design space, where the *x*-axis represents the resonance frequency and the *y*-axis denotes the total bandwidth. For the subset with a mass ratio of 7.0, four representative metastructures were highlighted: the red structures showed no absorption bandwidth, the blue structures presented a single absorption bandwidth, the green designs exhibited two absorption bandwidths, and the orange one revealed three. Interestingly, both the best- and worst-performing metastrucures in terms of vibration attenuation possessed only one absorption bandwidth, yet differ substantially in resonance frequency. This demonstrated that the number of absorption bandwidths alone is not a reliable predictor of attenuation performance. Within this subset, the best-performing metastructure in terms of resonance frequency achieved an attenuation range of 62.12 %. Another design, although exhibiting a slightly higher resonance frequency, presented a larger number of frequency points with transmissibility below 0.01. These results highlight the considerable diversity in dynamic behavior achievable for a fixed mass.

To further illustrate the potential of the generated metastructures, a comparison was conducted with two traditional designs: an homogeneous solid block and a honeycomb structure. For a meaningful comparison, both reference structures were designed to achieve the same mass ratio of 7. Under this constraint, the solid block corresponded to a square section with a side length of 2.52 cm, while

the honeycomb structure was generated using the classical Ashby and Gibson unit-cell parameterization [94]

The transmissibility responses of the homogeneous block and the honeycomb structure are shown in Fig. 5d alongside those of the best- and worst-performing metastructures. The homogeneous block exhibited a resonance peak at 2542 Hz and showed no absorption bandwidth within the investigated frequency range. The honeycomb structure displayed a resonance frequency of 824 Hz and an attenuation bandwidth of 14.22%, with attenuation beginning around 10 kHz. Overall, the honeycomb design performed worse than all generated metastructures, although it achieved a slightly larger attenuation range than three of the ten metastructures with the same mass ratio.

Moreover, despite their similar geometrical configurations, these generated metastructures displayed markedly different dynamic behaviors, suggesting their strong potential for adaptive applications. Each of these designs could be efficiently identified using their associated metrics. Their distinct transmissibility curves, illustrated in Fig. 5d, clearly emphasized variations in resonance frequency and total bandwidth between the most and least effective designs, as Designs 1 and 2, respectively.

5. Conclusions

In this paper, a computational design framework was introduced to both generate metastructures and evaluate them from a vibration attenuation standpoint. A generative design approach based on layered shape grammar rules was developed to create a large library of metastructures, while their dynamic response were assessed using FE simulations. The numerical model was validated experimentally, establishing confidence in the predictive accuracy of the simulation workflow. The use of shape grammar rules provided a systematic and flexible means of enriching the design process. By combining geometric control points with rule-based parameters, the proposed method generated a large set of unique structure topologies. This formulation not only enhanced the expressiveness of the design space but also offered a scalable route toward 3D metastructure generation, thereby paving the way for advanced data-driven design strategies in structure engineering.

To compute transmissibility, a fully automated pipeline was implemented, starting with a geometry generation script within Rhinoceros 7/Grasshopper® environment, followed by meshing in Gmsh, and then with a numerical simulation using a in-house code within FEniCSx FE framework. The validation against experimental data for VeroClear™-based metastructures confirmed the robustness of this workflow.

Analysis of the generated designs revealed that configurations combining all geometric parameters achieved a broader range of dynamic responses, including the emergence of wide absorption bandwidths. A dataset comprising 5000 metastructures was constructed, providing a valuable resource for future inverse design and machine learning applications. Several structures with identical mass ratios have exhibited distinct resonance frequencies, bandwidths and have shown better transmissibility performance than traditional designs. Moreover, these metastructures suggest the potential for adaptive or tunable vibration attenuation systems. Future research will extend this framework along multiple directions. First, the simulation pipeline will be generalized to handle full 3D metastructure analyses within the FEniCSx environment. Second, the influence of a higher mass will be studied to lower the resonance frequencies of the generated metastructures. Third, the developed dataset could enable applications in 4D printing and programmable materials, where metastructures dynamically adapt their geometry or stiffness in response to varying vibration conditions. Such capabilities could ultimately lead to intelligent, reconfigurable structures optimized for adaptive vibration mitigation and stealth performance.

CRediT authorship contribution statement

Robin Turlin: Writing – original draft, Methodology, Investigation, Formal analysis, Data curation, Conceptualization. **Thibaut Hirschler:** Writing – review & editing, Validation, Supervision, Software, Methodology, Formal analysis, Conceptualization. **Théo Calais:** Writing – review & editing, Validation, Methodology. **Hichem Seriket:** Writing – review & editing, Visualization, Software, Methodology. **Gaël Chevallier:** Writing – review & editing, Validation, Methodology, Formal analysis, Data curation. **Mahdi Bodaghi:** Writing – review & editing, Validation, Supervision, Methodology, Formal analysis, Conceptualization. **Frédéric Demoly:** Writing – review & editing, Validation, Supervision, Methodology, Investigation, Funding acquisition, Conceptualization.

Declaration of competing interest

The authors declare that they have no known competing financial interests or personal relationships that could have appeared to influence the work reported in this paper.

Acknowledgments

Appendix A. Finite element analysis

This appendix gives more details on the formulation and the numerical solving associated to problem (2). Particularly, we describe the algebraic form as the problem, and how it is solved in our implementation.

Coupling operator. The displacement coupling Eq. (2e) can be written in a matrix–vector fashion. In the general three-dimensional case, the rigid-body motion at the interface Γ_t can be expressed as:

$$\boldsymbol{u}_1(\mathrm{x},t) = \underbrace{\begin{bmatrix} \mathbf{1}_3 & \boldsymbol{R}(\mathrm{x}) \end{bmatrix}}_{\boldsymbol{B}^\top(\mathrm{x})} \begin{pmatrix} \boldsymbol{u}_2(t) \\ \boldsymbol{\theta}_2(t) \end{pmatrix},$$

$$\boldsymbol{R}(\mathrm{x}) = \begin{bmatrix} \boldsymbol{r}(\mathrm{x}) \end{bmatrix}_\times = \begin{bmatrix} 0 & r_z(\mathrm{x}) & -r_y(\mathrm{x}) \\ -r_z(\mathrm{x}) & 0 & r_x(\mathrm{x}) \\ r_y(\mathrm{x}) & -r_x(\mathrm{x}) & 0 \end{bmatrix},$$

where $\mathbf{1}_3$ is the 3×3 identity matrix, and $r_x(\mathrm{x})$ is the x-component of vector $\boldsymbol{r}(\mathrm{x})$, and similarly for y and z. Eventually, we can write this coupling condition component-wise in 2D:

$$\begin{pmatrix} u_1^x(\mathrm{x},t) \\ u_1^y(\mathrm{x},t) \end{pmatrix} = \underbrace{\begin{bmatrix} 1 & 0 & -r_y(\mathrm{x}) \\ 0 & 1 & -r_x(\mathrm{x}) \end{bmatrix}}_{\boldsymbol{B}^\top(\mathrm{x})} \begin{pmatrix} u_2^x(t) \\ u_2^y(t) \\ \theta_2^z(t) \end{pmatrix}.$$

Let us introduce d' such that the shape of $\boldsymbol{B}(\mathrm{x})$ is $d' \times d$. Thus $d' = 3$ when $d = 2$, and $d' = 6$ when $d = 3$.

We denote by Ω_1^h the meshed domain and by $\mathrm{x}_t^k, k = 1, \ldots, n_t$ the coordinate vectors of all FE nodes located on the top interface Γ_t (see Fig. 2(a)). After such a FE discretization step, we can define the following (discrete) coupling operator:

$$\mathbf{B} = \begin{bmatrix} \boldsymbol{B}(\mathrm{x}_t^1) & \boldsymbol{B}(\mathrm{x}_t^2) & \ldots & \boldsymbol{B}(\mathrm{x}_t^{n_t}) \end{bmatrix}, \quad \mathbf{B} \in \mathbb{R}^{d' \times n_t d},$$

This coupling operator is used to impose the continuity of the displacement (and acceleration), i.e., Eq (2e), as follows:

$$\mathbf{u}_t(t) = \mathbf{B}^\top \begin{pmatrix} \boldsymbol{u}_2(t) \\ \boldsymbol{\theta}_2(t) \end{pmatrix}, \quad \ddot{\mathbf{u}}_t(t) = \mathbf{B}^\top \begin{pmatrix} \ddot{\boldsymbol{u}}_2(t) \\ \ddot{\boldsymbol{\theta}}_2(t) \end{pmatrix}, \tag{4}$$

where $\mathbf{u}_t \in \mathbb{C}^{n_t d}$ is the vector of degrees of freedom associated with the "top" nodes of Ω_1^h. Interestingly, the exact same operator enables

to write the dynamic equilibrium of the item of mass, i.e., Eq. (2c) and (2d). If we denote by $\mathbf{f}_t$ the external (nodal) load vector that acts on the top DOF $\mathbf{u}_t$, then the dynamic equilibrium of the mounted mass reads in algebraic form as:

$$\underbrace{\begin{bmatrix} m_2 \mathbf{1}_d & \\ & \mathbf{I}_2 \end{bmatrix}}_{\mathbf{M}_2} \underbrace{\begin{pmatrix} \ddot{\boldsymbol{u}}_2(t) \\ \ddot{\boldsymbol{\theta}}_2(t) \end{pmatrix}}_{\ddot{\mathbf{d}}_2(t)} = -\mathbf{B}\,\mathbf{f}_t(t). \tag{5}$$

Linear system to be solved. Considering the split into top, internal and bottom DOF denoted $\mathbf{u}_t, \mathbf{u}_i, \mathbf{u}_b$, respectively, the dynamic equilibrium of the metastructures reads as:

$$\begin{bmatrix} \mathbf{M}_{tt} & \mathbf{M}_{ti} \\ \mathbf{M}_{it} & \mathbf{M}_{ii} \end{bmatrix} \begin{pmatrix} \ddot{\mathbf{u}}_t(t) \\ \ddot{\mathbf{u}}_i(t) \end{pmatrix} + (1 + \mathrm{i}\eta) \begin{bmatrix} \mathbf{K}_{tt} & \mathbf{K}_{ti} \\ \mathbf{K}_{it} & \mathbf{K}_{ii} \end{bmatrix} \begin{pmatrix} \mathbf{u}_t(t) \\ \mathbf{u}_i(t) \end{pmatrix}$$
$$= \begin{pmatrix} \mathbf{f}_t(t) \\ \mathbf{0}_i \end{pmatrix} - \begin{bmatrix} \mathbf{M}_{tb} \\ \mathbf{M}_{ib} \end{bmatrix} \ddot{\mathbf{u}}_b(t) - (1 + \mathrm{i}\eta) \begin{bmatrix} \mathbf{K}_{tb} \\ \mathbf{K}_{ib} \end{bmatrix} \mathbf{u}_b(t). \tag{6}$$

where $\mathbf{M}_{tt}, \mathbf{M}_{ti}, \ldots$ and $\mathbf{K}_{tt}, \mathbf{K}_{ti}, \ldots$ are corresponding mass and stiffness sub-matrices (standard FE operators), respectively. By substituting the coupling Eqs. (4) and (5) into Eq. (6), we end up with the following coupled system of equations that describes the dynamic equilibrium of the full mounting device (metastructure + item of mass):

$$\underbrace{\begin{bmatrix} \mathbf{M}_2 + \mathbf{B}^\top \mathbf{M}_{tt} \mathbf{B} & (\mathbf{M}_{it} \mathbf{B})^\top \\ \mathbf{M}_{it} \mathbf{B} & \mathbf{M}_{ii} \end{bmatrix}}_{\bar{\mathbf{M}}} \underbrace{\begin{pmatrix} \ddot{\mathbf{d}}_2(t) \\ \ddot{\mathbf{u}}_i(t) \end{pmatrix}}_{\ddot{\mathbf{d}}(t)} + \underbrace{\begin{bmatrix} \mathbf{B}^\top \mathbf{K}_{tt}^* \mathbf{B} & (\mathbf{K}_{it}^* \mathbf{B})^\top \\ \mathbf{K}_{it}^* \mathbf{B} & \mathbf{K}_{ii}^* \end{bmatrix}}_{\bar{\mathbf{K}}} \underbrace{\begin{pmatrix} \mathbf{d}_2(t) \\ \mathbf{u}_i(t) \end{pmatrix}}_{\mathbf{d}(t)}$$
$$= -\begin{bmatrix} \mathbf{B}^\top \mathbf{M}_{tb} \\ \mathbf{M}_{ib} \end{bmatrix} \ddot{\mathbf{u}}_b(t) - \begin{bmatrix} \mathbf{B}^\top \mathbf{K}_{tb}^* \\ \mathbf{K}_{ib}^* \end{bmatrix} \mathbf{u}_b(t).$$

Here, we define $\mathbf{K}_{tt}^* = (1 + \mathrm{i}\eta)\mathbf{K}_{tt}$, and identically for other stiffness sub-matrices (these sub-matrices have now complex-valued entries).

Finally, we can reformulate the problem to be solved by considering a moving coordinate system that follows the harmonic displacement imposed at the bottom DOF. This leads to the linear system presented in Eq. (3) which we recall here:

$$\bar{\mathbf{D}}(\omega)\,\mathbf{d}^{\mathrm{rel}} = \omega^2 \bar{\mathbf{M}}\,\mathbf{d}^0,$$

where the dynamic stiffness matrix $\bar{\mathbf{D}}(\omega) \in \mathbb{C}^{n_{\mathrm{free}} \times n_{\mathrm{free}}}$ is given by $\bar{\mathbf{D}}(\omega) = \bar{\mathbf{K}} - \omega^2 \bar{\mathbf{M}}$, and the vector $\mathbf{d}^0 \in \mathbb{R}^{n_{\mathrm{free}}}, n_{\mathrm{free}} = n_i d + d'$, simply reads as:

$$(\mathbf{d}^0)^\top = U_{\mathrm{in}} \big(\mathbf{e}_y^\top \underbrace{0, \ldots, 0}_{1 \text{ or } 3 \text{ times}} \underbrace{\mathbf{e}_y^\top, \ldots, \mathbf{e}_y^\top}_{n_i \text{ times}} \big).$$

Modal superposition. The output vibration magnitude $U_{\mathrm{out}}(\omega)$ needs to be evaluated over a range of frequencies $\omega \in [\omega_{\mathrm{min}}, \omega_{\mathrm{max}}]$. This means that problems of the form given by Eq. (3) need to be solved (and eventually built) multiple times. These multiple analyzes can be performed efficiently by first (and only once) building the mass and stiffness matrices $\bar{\mathbf{M}}$ and $\bar{\mathbf{K}}$, secondly by performing a natural frequency analysis, and finally solving the forced vibration problem within the reduced space made up of the computed eigenmodes.

More specifically, we compute n_M eigenmodes denoted $(\omega_k, \mathbf{v}_k) \in \mathbb{R} \times \mathbb{R}^{n_{\mathrm{free}}}$, solution of:

$$\mathfrak{Re}(\bar{\mathbf{K}})\mathbf{v}_k = \omega_k^2 \bar{\mathbf{M}}\mathbf{v}_k, \quad k = 1, \ldots, n_M, \tag{7}$$

where operator $\mathfrak{Re}$ extract the real part of the stiffness matrix. The eigenmodes of interest are those with an eigenfrequency that lies in (or close to) the range of interest. The eigenvectors can then be stacked in a reduced basis matrix $\mathbf{V} = [\mathbf{v}_1, \ldots, \mathbf{v}_{n_M}] \in \mathbb{R}^{n_{\mathrm{free}} \times n_M}$ and the modal superposition approach leads to approximate the solution as a linear combination of these modes, i.e.:

$$\mathbf{d}^{\mathrm{rel}}(\omega) \approx \mathbf{V}\boldsymbol{\alpha}(\omega),$$

where the modal amplitudes $\boldsymbol{\alpha}(\omega) \in \mathbb{C}^{n_M}$ are now solution of the following (small) n_M-by-n_M complex-valued linear system:

$$\big[\mathbf{V}^\top \bar{\mathbf{D}}(\omega) \mathbf{V} \big] \boldsymbol{\alpha} = \omega^2 \mathbf{V}^\top \bar{\mathbf{M}}\,\mathbf{d}^0.$$
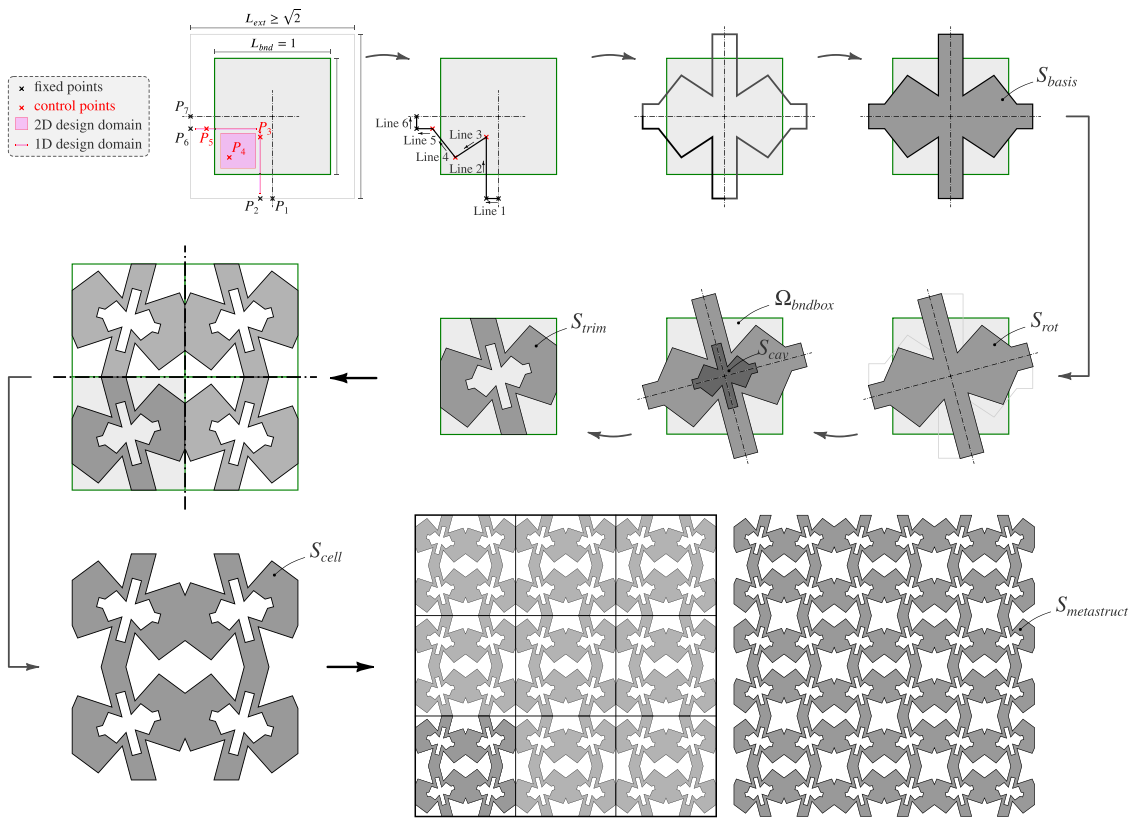
Fig. 6. Main steps of the presented generative design methodology: from a set of points to the surface representing a metastructure. The different steps and mentioned geometric entities are also reported in Algo. 1.

It can be solved analytically due to the orthogonality properties of the eigenmodes:

$$\alpha_k(\omega) = \mathbf{v}_k^\top \bar{\mathbf{M}} \mathbf{d}^0 \frac{\omega^2}{(1 + i\eta)\omega_k^2 - \omega^2}, \quad k = 1, \ldots, n_M. \tag{8}$$

Evaluating the transmissibility via Eq. (8) for a large set of excitation frequency $\omega \in [\omega_{\min}, \omega_{\max}]$ is then much faster than doing it blindly via Eq. (3). Lastly, once the solution $\mathbf{d}^{\text{rel}} \in \mathbb{C}^{n_{\text{free}}}$, one can get the output magnitude U_{out} needed to evaluate the transmissibility as:

$$U_{\text{out}}(\omega) = |U_{\text{in}} + \mathbf{u}_2^{\text{rel}}(\omega) \cdot \mathbf{e}_y|,$$

where $\mathbf{u}_2^{\text{rel}} \in \mathbb{C}^d$ is the first sub-vector of $\mathbf{d}^{\text{rel}}$.

Appendix B. Shape-grammar-based design workflow

Geometric modeling steps. One can find in Fig. 6 the different modeling steps, starting from a set of fixed and controls points to the final surface. It involves the fundamental shape grammar rules as discussed in Section 2.2. Along with the illustration from Fig. 6, one can find in Algo. 1 all these successive operations written in as a pseudo-algorithm.

An extension to 3D metastructure design. The transition from 2D to 3D metastructures can be achieved by extending the shape grammar rules. This extension introduces the extrusion rule, an additional operation that imparts volume to planar geometries and increases the dimensionality of the design parameter space. Two complementary strategies can be defined for the generation of 3D metastructures, each corresponding to a distinct logic of spatial composition: union-based aggregation and intersection-based integration. Together, these strategies considerably enrich the generative potential of the framework, enabling the synthesis of a large space of topologically distinct metastructures from a single parameter basis.

In the union-based aggregation, the union rule merges two or more volumetric entities into a single continuous structure, ensuring material continuity across adjacent domains. The extrusion rule is applied to give thickness to 2D unit cells, after which successive union operations combine extruded cells from different planes (xy, xz, and yz). As illustrated in Fig. 7, this process yields several different configurations depending on how many planes are merged. A fourth configuration can be generated by applying the rule simultaneously across all extruded layers, producing a fully interconnected 3D metastructure. The extrusion factor, defined as the distance above and below the mid-plane of the unit cell domain, can take asymmetric values, allowing geometric imbalance and structural anisotropy to be intentionally introduced.

The intersection-based integration builds upon the intersection rule, which extracts the common domain of two or more shapes, allowing for selective refinement and system deduction of design complexity. In this second strategy, the unit cell is completely extruded along its third axis to occupy its entire bounding volume. Intersection operations are then applied between multiple extruded layers or across the three principal planes (xy, xz, and yz), generating morphologies that exhibit spatial selectivity and complex internal cavities.

As with the union-based strategy, multiple structural configurations emerge from the same set of shape grammar rules, highlighting the modular and scalable nature of the systematic design process.

Appendix C. Supplementary data

Supplementary material related to this article can be found online at https://doi.org/10.1016/j.ijmecsci.2026.111469.
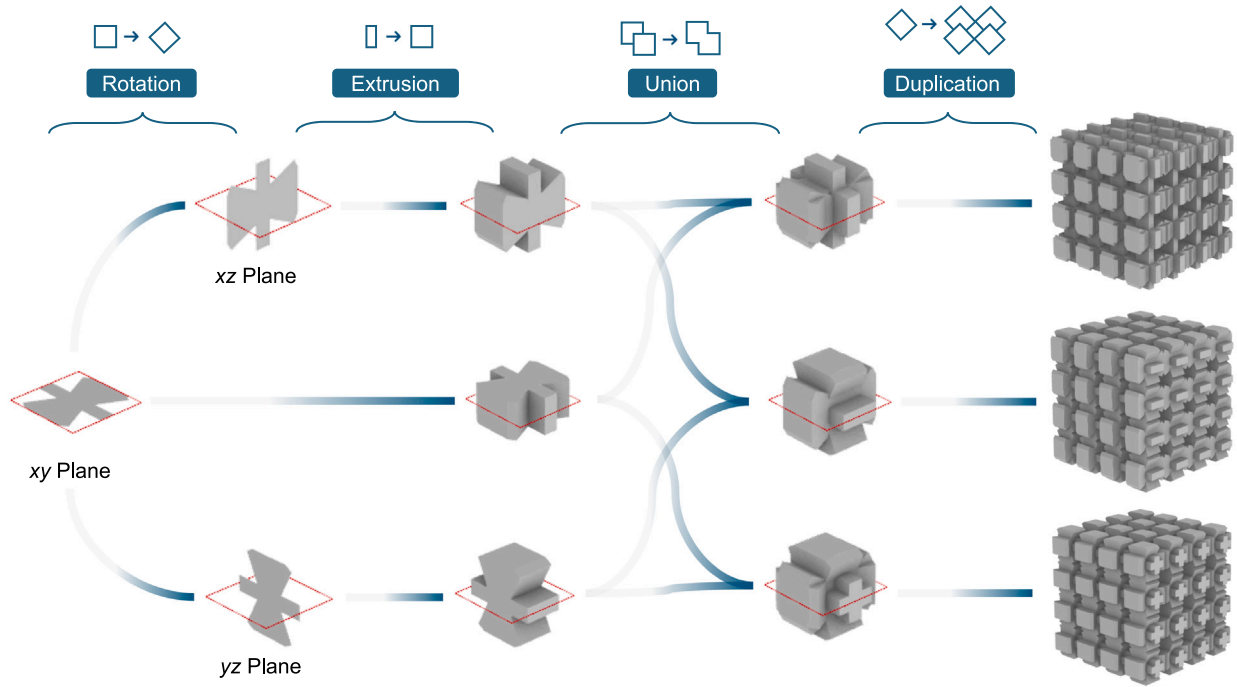
Fig. 7. Systematic design workflow for 3D metastructures generation based on shape grammar rules. The process begins with a 2D base unit cell that undergoes a sequence of formal operations – rotation, extrusion, and union – to progressively increase geometric complexity. The duplication rule is then applied to replicate the resulting 3D unit cell periodically within the design domain, forming a complete 3D metastructure. Different combinations of the rotation, extrusion, and union rules yield diverse topologies.

Algorithm 1: Procedure for the generative design of 2D-metastructures as illustrated in Fig. 6.

Input: Geometrical parameters μ
Output: Metastructure

begin // Baseline surface.
  // Set of points
  for $k = 1, n$ **do**
    case *Fixed point* **do**
      | $coord_k = (x_k, y_k), \quad coord_k \in \Omega_{ext}^-$
    case *Control point* **do**
      | $coord_k = f(\mu), \quad coord_k \in \Omega_{design}$
    $P_k \leftarrow \text{Point}(coord_k)$
  end
  // Wireframe construction
  $Lines \leftarrow \bigcup_{k=1}^{n-1} \text{Line}(P_k, P_{k+1})$
  $Lines \leftarrow Lines \cup \text{Sym}(Lines, Plane_{Oyz})$
  $Lines \leftarrow Lines \cup \text{Sym}(Lines, Plane_{Oxz})$
  // Generate surface
  $S_{basis} \leftarrow \text{Surface}(Lines)$
end
begin // Unit cell.
  | $S_{rot} \leftarrow \text{Rotate}(S_{basis}, \mu_{rot})$
  | $S_{cav} \leftarrow \text{Scale}(S_{rot}, \mu_{scale})$
  | $S_{trim} \leftarrow S_{rot} \setminus S_{cav}$
  | $S_{trim} \leftarrow S_{trim} \cap \Omega_{bndbox}$
  | $S_{cell} \leftarrow S_{trim} \cup \text{Sym}(S_{trim}, Plane_{O'yz})$
  | $S_{cell} \leftarrow S_{cell} \cup \text{Sym}(S_{cell}, Plane_{O'xz})$
end
begin // Metastructure assembly.
  | $S_{metastruct} \leftarrow \text{GridDuplicate}(S_{cell}, \mu_{n_x}, \mu_{n_y})$
end

Data availability

The processed data required to reproduce the above findings are available to download from

Computed Dataset of Viscoelastic Metastructures for Vibration Attenuation (Original data) (Zenodo)

References

[1] Özden MC, Gürkan AY, Özden YA, Canyurt TG, Korkut E. Underwater radiated noise prediction for a submarine propeller in different flow conditions. Ocean Eng 2016;126:488–500.

[2] Huo L, m. Fei S. Design on the fairwater shape and its influence on the radiation noise of submarines. J Vibroengineering 2016;18:5378–89.

[3] Ginoux J-M, Bertinier M. La maîtrise de la discrétion acoustique dans un programme de navire. Acoust Tech 2011.

[4] Yang T, Wu L, Li X, Zhu M, Liu Z, Brennan MJ. Combining active control and synchrophasing for vibration isolation of a floating raft system: An experimental demonstration. J Low Freq Noise, Vib Act Control 2021;40:1105–14.

[5] Dai W, Li T, Wang L, Zhu X, Shi B, Yang J. Performance enhancement of floating raft system by exploiting geometric nonlinearity and motion constraint in vibration isolators. Ocean Eng 2024;314:119656.

[6] Chen F, Chen Y, Hua H. Coupled vibration characteristics of a submarine propeller-shaft-hull system at low frequency. J Low Freq Noise, Vib Act Control 2020;39:258–79.

[7] Fang Y, Zuo Y, Xia Z. Study on design method and vibration reduction characteristic of floating raft with periodic structure. IOP Conf Ser: Mater Sci Eng 2018;322:042025.

[8] Xue Q, Wang Y, Wang C, Hu Q, Zou G, Chen M, He C. Experimental and simulation study on vibration transmission characteristics and vibration isolation effect of a new floating raft vibration isolation system. J Mar Sci Eng 2025;13:254.

[9] Qiu Y, Xu W, Hu Z, Fu J, He M. Review of lightweight vibration isolation technologies for marine power devices. Shock Vib 2024;2024:1076935.

[10] Li L, Li B, Xu Z. Design of distributed dynamic absorbers for vibration suppression of panel structures. Acta Mech Sin 2024;40:523521.

[11] Fu J, Xu W, Qiu Y, Hu Z. Broadband vibration attenuation in marine mounting systems using multiple dynamic vibration absorbers. Ships Offshore Struct 2025;1–11.

[12] Ke Y, Yin J, He Y, Zheng Z, Wang Q, Geng X, Yu D, Wen J. Locally multi-resonant meta-shells for broadband vibration suppression. Int J Mech Sci 2024;278:109452.

[13] Lu Z, Wang Z, Masri SF, Lu X. Particle impact dampers: Past, present, and future. Struct Control Health Monit 2018;25:e2058.

[14] Ma Z, Zhou R, Yang Q. Recent advances in quasi-zero stiffness vibration isolation systems: An overview and future possibilities. Machines 2022;10:813.

[15] Winberg M, Hansen C, Claesson I, Li X. Active control of engine vibrations in a collins class submarine. Technical Report, Blekinge Institute of Technology; 2003.

[16] Butaud P, Renault D, Verdin B, Ouisse M, Chevallier G. In-core heat distribution control for adaptive damping and stiffness tuning of composite structures. Smart Mater Struct 2020;29:065002.

[17] Roberjot J, Sadoulet-Reboul E, Peyret N, Bachy E, Arnould C, Collard E, Jaboviste K, Chevallier G. Proof of concept of a tunable suspension using a temperature-driven polymer. Smart Mater Struct 2025;34:105025.

[18] Bachy E, Jaboviste K, Sadoulet-Reboul E, Peyret N, Chevallier G, Arnould C, Collard E. Investigations on the performance and the robustness of a metab-sorber designed for structural vibration mitigation. Mech Syst Signal Process 2022;170:108830.

[19] Yan G, Qi W-H, Lu J-J, Liu F-R, Yan H, Zhao L-C, Wu Z-Y, Zhang W-M. Bio-inspired multi-joint-collaborative vibration isolation. J Sound Vib 2024;568:118089.

[20] Zhou W, Li Y, Zhou J, Peng Y. Limb-inspired quasi-zero stiffness structure for ultralow-frequency vibration attenuation. Int J Mech Sci 2024;274:109251.

[21] Wu W, Jiang T, Sui G, Shan X, Sun C, Xie X, Zhou C. Bioinspired frog adaptive-mass quasi-zero stiffness vibration isolator. Int J Mech Sci 2025;301:110509.

[22] Jaboviste K, Sadoulet-Reboul E, Peyret N, Arnould C, Collard E, Chevallier G. On the compromise between performance and robustness for viscoelastic damped structures. Mech Syst Signal Process 2019;119:65–80.

[23] j. Xin Y, n. Huang R, Li P, Yan H, j. Dong X, Yan Q, t. Sun Y, l. Cheng S, x. Zhao Q. Labyrinth acoustic metamaterials with fractal structure based on Hilbert curve. Phys B 2023;667:415150.

[24] Shi P, Chen Y, Wei J, Xie T, Feng J, Sareh P. Design and low-velocity impact behavior of an origami-bellow foldcore honeycomb acoustic metastructure. Thin-Walled Struct 2024;197:111607.

[25] Lu C, Shao Z, Chen Y, Feng J, Sareh P. Designing optimally slender origami-inspired tubular structures for enhanced energy absorption. Eur J Mech A Solids 2026;116:105909.

[26] Guo X, Li X, Wang E, Fuh JY, Lu WF, Zhai W. Bioinspired hierarchical diamond triply periodic minimal surface lattices with high energy absorption and damage tolerance. Addit Manuf 2023;76:103792.

[27] Ren F, Wang L, Liu H. Low frequency and broadband vibration attenuation of a novel lightweight bidirectional re-entrant lattice metamaterial. Mater Lett 2021;299:130133.

[28] Ren X, Sun L, Zhang Y, Jiang W, Zhao A, Xie Y. A novel re-entrant hon-eycomb metamaterial with enhanced auxetic behavior. Smart Mater Struct 2022;31:095024.

[29] Wang S, Wang A, Wu Y, Li X, Sun Y, Zhang Z, Ding Q, Ayalew GD, Ma Y, Lin Q. Ultra-wide band gap and wave attenuation mechanism of a novel star-shaped chiral metamaterial. Appl Math Mech 2024;45:1261–78.

[30] Wang G, Wan S, Hong J, Li L, Liu S, Li X. In plane mechanical properties of hexagonal V-chiral and tri-chiral metamaterials. Eng Struct 2024;315:118502.

[31] Zhao P, Zhang K, Qi L, Deng Z. 3D chiral mechanical metamaterial for tailored band gap and manipulation of vibration isolation. Mech Syst Signal Process 2022;180:109430.

[32] Liu X, Zhang K, Shi H, Hong F, Liu H, Deng Z. Origami-inspired metamaterial with compression–twist coupling effect for low-frequency vibration isolation. Mech Syst Signal Process 2024;208:111076.

[33] Ruzzene M. Vibration and sound radiation of sandwich beams with honeycomb truss core. J Sound Vib 2004;277:741–63.

[34] Ruan H, Li D. Band gap characteristics of bionic acoustic metamaterials based on spider web. Eng Struct 2024;308:118003.

[35] d. Li X, l. Cheng S, y. Li J, t. Sun Y, Wang S, j. Xin Y, Yan Q, Ding Q, Yan H. Analysis of vibration and noise reduction performance of 3D flower-shaped resonance structure with low-frequency bandgap. Phys B 2024;680:415806.

[36] Guo J, Li Y, Xiao Y, Fan Y, Yu D, Wen J. Multiscale modeling and design of lattice truss core sandwich metastructures for broadband low-frequency vibration reduction. Compos Struct 2022;289:115463.

[37] Li H, Hu Y, Huang H, Chen J, Zhao M, Li B. Broadband low-frequency vibration attenuation in 3D printed composite meta-lattice sandwich structures. Compos Part B: Eng 2021;215:108772.

[38] Zhang K, Ding B, Hong F, Liu H, Yu J, Deng Z. A compressible square-frustum sandwich structure for low-frequency vibration suppression: Numerical and experimental analyses. Thin-Walled Struct 2023;188:110783.

[39] Li Z-Y, Ma T-X, Wang Y-Z, Li F-M, Zhang C. Vibration isolation by novel meta-design of pyramid-core lattice sandwich structures. J Sound Vib 2020;480:115377.

[40] Cheng Z, Zhang X, Yan K, Zhao Y, Cui J. An improved BCC lattice structure for vibration isolation in extreme environment. Adv Mech Eng 2024;16:16878132241297489.

[41] Fan H, Yang L, Tian Y, Wang Z. Design of metastructures with quasi-zero dynamic stiffness for vibration isolation. Compos Struct 2020;243:112244.

[42] Zhao J. Integrated design of a lightweight metastructure for broadband vibration isolation. Int J Mech Sci 2023.

[43] Zhou H, Gao J, Chen Y, Shen Z, Lv H, Sareh P. A quasi-zero-stiffness vibration isolator inspired by kresling origami. Structures 2024;69:107315.

[44] He R, Chen Y, Shi J, Bai Y, Feng J. Programming morphological and me-chanical performance of cyclic ori-kirigami via design-feasible parameter space. Thin-Walled Struct 2025;207:112706.

[45] Liu W, Yan S, Meng Z, Wu L, Xu Y, Chen J, Sun J, Zhou J. Programmable quasi-zero-stiffness metamaterials. Engineering 2025;47:160–7.

[46] Li L, Yang F, Liu S, Guo Z, Han D, Xia Y, Wang L, Fan H. Design of quasi-zero-stiffness metamaterials with ultra-wideband vibration isolation performance. Int J Mech Sci 2025;300:110440.

[47] Liu W, Wu L, Zhang J, Sun J, Zhou J. Metamaterial springs for low-frequency vibration isolation. J Mater 2025;11:100884.

[48] Ravanbod S, Rahmani K, Branfoot C, Karmel S, Haque A, Lidgett M, Shahidi AM, Alderson A, Bodaghi M. Biomimetic composite meta-stabilisers with pro-grammable multi-directional quasi-zero stiffness and vibration isolation. Mater Today Adv 2025;28:100661.

[49] Lin Q, Zhou J, Wang K, Xu D, Wen G, Wang Q, Cai C. Low-frequency locally resonant band gap of the two-dimensional quasi-zero-stiffness metamaterials. Int J Mech Sci 2022;222:107230.

[50] Cai C, Zhou J, Wu L, Wang K, Xu D, Ouyang H. Design and numerical validation of quasi-zero-stiffness metamaterials for very low-frequency band gaps. Compos Struct 2020;236:111862.

[51] Jiang W, Yin G, Xie L, Yin M. Multifunctional 3D lattice metamaterials for vibration mitigation and energy absorption. Int J Mech Sci 2022;233:107678.

[52] d. Li X, l. Cheng S, Zhang Q, t. Sun Y, j. Xin Y, Bin W. Novel three-dimensional acoustic metamaterials with low-frequency bandgap and strong vibration and noise attenuation. Phys B 2024;689:416213.

[53] Li Y, Yan G. Vibration characteristics of innovative reentrant-chiral elastic metamaterials. Eur J Mech A Solids 2021;90:104350.

[54] Jiang W, Yin M, Liao Q, Xie L, Yin G. Three-dimensional single-phase elastic metamaterial for low-frequency and broadband vibration mitigation. Int J Mech Sci 2021;190:106023.

[55] Abubakar M, Shi H, Bai X, Yang T, Zhang K, Sun X. Vibration attenuation using a 3D cubic re-entrant metamaterial structure with tunable bandgaps induced by variations in the re-entrant angle. EPJ Appl Metamaterials 2025;12:5.

[56] Wu J, Zhang X, Liu K, Cheng Q, He Y, Yin J, Yu D, Wen J. Auxetic hierarchical metamaterials with programmable dual-plateau energy absorption and broadband vibration attenuation. Eng Struct 2025;330:119912.

[57] Hankin H, Gagen J, Peters W, Crann A, Chen Y, Fares S, Sareh P. Airless tires: Structural concepts, mechanical design, and application prospects. Mater Des 2025;253:113933.

[58] Sangiuliano L, Reff B, Palandri J, Wolf-Monheim F, Pluymers B, Deckers E, Desmet W, Claeys C. Low frequency tyre noise mitigation in a vehicle using metal 3D printed resonant metamaterials. Mech Syst Signal Process 2022;179:109335.

[59] Wang T, Wang G, Chen Z, Zhu Z, Lim CW. An innovative spider-like multi-origami metamaterial for tunable low-frequency vibration attenuation. Nonlinear Dynam 2024.

[60] Li L, Wu J, Yang F, Li P, Lu G, Fan H, Zhao J, Zhang N, Yang Q. Mechanisms of low-frequency bandgap formation and energy absorption of three-dimensional nested hybrid lattice structures. Compos Part B: Eng 2025;291:112045.

[61] An X, Lai C, Fan H, Zhang C. 3D acoustic metamaterial-based mechanical metalattice structures for low-frequency and broadband vibration attenuation. Int J Solids Struct 2020;191–192:293–306.

[62] Elmadih W, Chronopoulos D, Syam WP, Maskery I, Meng H, Leach RK. Three-dimensional resonating metamaterials for low-frequency vibration attenuation. Sci Rep 2019;9:11503.

[63] Zhang R, Ding W, Fang B, Feng P, Wang K, Chen T, Zhu J. Syndiotactic chiral metastructure with local resonance for low-frequency vibration isolation. Int J Mech Sci 2024;281:109564.

[64] Tao Z, Ren X, Zhao AG, Sun L, Zhang Y, Jiang W, Han D, Zhang XY, Xie YM. A novel auxetic acoustic metamaterial plate with tunable bandgap. Int J Mech Sci 2022;226:107414.

[65] Hao S, Sheng H, Li H, Zhang Z, Ding Q. Broadband vibration isolation of floating raft system via sandwich metamaterial with acoustic black hole absorbers. Ocean Eng 2025;341:122600.

[66] An X, Lai C, He W, Fan H. Three-dimensional meta-truss lattice com-posite structures with vibration isolation performance. Extrem Mech Lett 2019;33:100577.

[67] Yang Y, Liu H-L, Yuan J-W, Kong W-L, Wan M, Zhang W-H. Development of an anti-vibration cutting tool combining the lattice structures infill with damping particles. Mech Syst Signal Process 2025;228:112425.

[68] Gao X, Wei J, Huo J, Wan Z, Li Y. The vibration isolation design of a re-entrant negative Poisson's ratio metamaterial. Appl Sci 2023;13:9442.

[69] Tomita S, Masutani T, Sato H. Locally resonant metamaterials damped by particles embedded through additive manufacturing. J Sound Vib 2025;596:118715.

[70] Ha CS, Yao D, Xu Z, Liu C, Liu H, Elkins D, Kile M, Deshpande V, Kong Z, Bauchy M, Zheng X. Rapid inverse design of metamaterials based on prescribed mechanical behavior through machine learning. Nat Commun 2023;14:5765.

[71] Fang B, Zhang R, Chen T, Wang W, Zhu J, Cheng W. Bandgap optimization and inverse design of labyrinth metamaterials for sound insulation. J Build Eng 2024;86:108898.

[72] Hu C, Wan Z, Li Z, Tan X, Wang L, Chen M. Inverse-designed metastructures with customizable low dynamic stiffness characteristics for low-frequency vibration isolation. Eur J Mech A Solids 2025;110:105515.

[73] Deng B, Zareei A, Ding X, Weaver JC, Rycroft CH, Bertoldi K. Inverse design of mechanical metamaterials with target nonlinear response via a neural accelerated evolution strategy. Adv Mater 2022;34:2206238.

[74] Zhang K, Guo Y, Liu X, Hong F, Hou X, Deng Z. Deep learning-based inverse design of lattice metamaterials for tuning bandgap. Extrem Mech Lett 2024;69:102165.

[75] Kang S, Song H, Kang H Seok, Bae B-S, Ryu S. Customizable metamaterial design for desired strain-dependent Poisson's ratio using constrained generative inverse design network. Mater Des 2024;247:113377.

[76] Jiang W, Zhu Y, Yin G, Lu H, Xie L, Yin M. Dispersion relation prediction and structure inverse design of elastic metamaterials via deep learning. Mater Today Phys 2022;22:100616.

[77] Li X, Ning S, Liu Z, Yan Z, Luo C, Zhuang Z. Designing phononic crystal with anticipated band gap through a deep learning based data-driven method. Comput Methods Appl Mech Engrg 2020;361:112737.

[78] Wan X-H, Zhang Y, Guo Q-H, Zheng L-Y. Deep learning-based inverse design of irregular phononic crystals. Int J Mech Sci 2025;297–298:110335.

[79] Nourian P, Azadi S, Oval R. Generative design in architecture: From mathematical optimization to grammatical customization. In: Kyratsis P, Manavis A, Davim JP, editors. Computational design and digital manufacturing. Cham: Springer International Publishing; 2023, p. 1–43. http://dx.doi.org/10.1007/978-3-031-21167-6_1, series Title: Management and Industrial Engineering. URL https://link.springer.com/10.1007/978-3-031-21167-6_1.

[80] Xu Y, Dong H-W, Wang Y-S. Topology optimization of programable quasi-zero-stiffness metastructures for low-frequency vibration isolation. Int J Mech Sci 2024;280:109557.

[81] Zhao H, Feng Y, Li W, Xue C. Numerical study and topology optimization of vibration isolation support structures. Int J Mech Sci 2022;228:107507.

[82] Wei Z, Chen J, Wei K. Generative deep learning for designing irregular metamaterials with programmable nonlinear mechanical responses. Int J Mech Sci 2025;291–292:110123.

[83] Prusinkiewicz P, Hanan J, Hammel M, Mech R. L-systems: from the theory to visual models of plants. Proceedings of the 2nd CSIRO Symposium on Computational Challanges in Life Sciences. CSIRO Publishing; 1996.

[84] Sun Ruoxi, Jia Jinyuan, Jaeger M. Intelligent tree modeling based on L-system. In: 2009 IEEE 10th international conference on computer-aided industrial design & conceptual design. Wenzhou, China: IEEE; 2009, p. 1096–100. http://dx.doi.org/10.1109/CAIDCD.2009.5375256, URL http://ieeexplore.ieee.org/document/5375256/.

[85] Mahabadi R Karimi, Chen Z, Ogren AC, Zhang H, Daraio C, Rudin C, Brinson LC. Graph-based design of irregular metamaterials. Int J Mech Sci 2025;295:110203.

[86] Wang X, Song Y, Tang P. Generative urban design using shape grammar and block morphological analysis. Front Archit Res 2020;9:914–24.

[87] Kielarova SW, Pradujphongphet P, Bohez ELJ. New interactive-generative design system: Hybrid of shape grammar and evolutionary design - an application of jewelry design. In: Tan Y, Shi Y, Buarque F, Gelbukh A, Das S, Engelbrecht A, editors. In: Advances in swarm and computational intelligence, vol. 9140, Cham: Springer International Publishing; 2015, p. 302–13. http://dx.doi.org/10.1007/978-3-319-20466-6_33, series Title: Lecture Notes in Computer Science. URL https://link.springer.com/10.1007/978-3-319-20466-6_33.

[88] Zimmermann L, Chen T, Shea K. A 3D, performance-driven generative design framework: automating the link from a 3D spatial grammar interpreter to structural finite element analysis and stochastic optimization. Artif Intell Eng Des Anal Manuf 2018;32:189–99.

[89] Nasiri S. Auxetic grammars: An application of shape grammar using shape machine to generate auxetic metamaterial geometries for fabricating sustainable kinetic panels. In: Yan C, Chai H, Sun T, Yuan PF, editors. Phygital intelligence. Singapore: Springer Nature Singapore; 2024, p. 114–24. http://dx.doi.org/10.1007/978-981-99-8405-3_10, series Title: Computational Design and Robotic Fabrication. URL https://link.springer.com/10.1007/978-981-99-8405-3_10.

[90] Ruiz-Montiel M, Belmonte M-V, Boned J, Mandow L, Millán E, Badillo AR, de-la Cruz J-L Pérez. Layered shape grammars. Comput-Aided Des 2014;56:104–19.

[91] Snowdon JC. Rubberlike materials, their internal damping and role in vibration isolation. J Sound Vib 1964.

[92] Geuzaine C, Remacle J-F. Gmsh: A 3-d finite element mesh generator with built-in pre- and post-processing facilities. Internat J Numer Methods Engrg 2009.

[93] Baratta IA, Dean JP, Dokken JS, Habera M, Hale JS, Richardson CN, Rognes ME, Scroggs MW, Sime N, Wells GN. DOLFINx: the next generation fenics problem solving environment. 2023, http://dx.doi.org/10.5281/ZENODO.10447666.

[94] Gibson LJ, Ashby MF. Cellular solids: structure and properties. second ed.. Cambridge, UK: Cambridge University Press; 1997.